Nitrogen at the Si-nanocrystal/SiO_2 interface and its influence on luminescence and interface defects

Daniel Hiller,[1] Silvana Goetze,[2] Frans Munnik,[3] Mihaela Jivanescu,[4] Jürgen W. Gerlach,[5] Jürgen Vogt,[6] Eckhard Pippel,[2] Nikolai Zakharov,[2] Andre Stesmans,[4] and Margit Zacharias[1]

[1]*IMTEK, Faculty of Engineering, Albert-Ludwigs-University Freiburg, Georges-Köhler-Allee 103, 79110 Freiburg, Germany*

[2]*Max Planck Institute of Microstructure Physics, Weinberg 2, 06120 Halle, Germany*

[3]*Forschungszentrum Dresden-Rossendorf e.V., Bautzner Landstrasse 400, 01328 Dresden, Germany*

[4]*Department of Physics, University of Leuven, Celestijnenlaan 200D, 3001 Leuven, Belgium*

[5]*Leibniz Institute of Surface Modification (IOM), Permoserstrasse 15, 04318 Leipzig, Germany*

[6]*Faculty of Physics and Earth Sciences, University of Leipzig, Linnéstrasse 5, 04103 Leipzig, Germany*

(Received 27 May 2010; published 1 November 2010)

The influence of the high-temperature annealing ambient, i.e., N_2 and Ar on size controlled Si nanocrystals (NCs) ranging from ~2 to ~6 nm embedded in SiO_2 has been investigated in detail. Generally, N_2 annealing is proven to be beneficial as the dangling bond density (P_b defects at the NC/SiO_2 interface) is about half, accompanied by a doubled photoluminescence (PL) intensity. The PL blueshift of N_2 annealed samples compared to Ar-annealed samples (N-blueshift) was found to be pronounced only for small NCs whereas it appears to be insignificant for larger NCs. The origin of this N-blueshift was previously attributed to a growth suppression of the NCs by the presence of N during the annealing process. However, no evidence for this assumption is found by time-resolved PL, as the luminescence decay times are similar despite considerable N-blueshift. The exact location of the N incorporated during annealing was investigated by time-of-flight-SIMS and electron-spin resonance. Besides the distinct N enrichment in the NC layer, the K^0 center ($^{\bullet}Si \equiv N_3$) was detected indicating the formation of an interfacial N layer at the NC/SiO_2 interface. Elastic recoil detection analysis enabled the quantification of the incorporated N as well as the excess Si. Combined with transmission electron microscopy analysis (determination of NC size) the calculation of the NC density per superlattice layer and the thickness of the interfacial N layer were achieved. It turns out that ~5×10^{14} N atoms cm^{-2} exist at the NC surface, which is well in accordance to the optimum value of the bulk Si/SiO_2 interface. These results strongly support our recently suggested explanation for the N-blueshift that is based on an increased NC band gap by the influence of interfacial N on the polarity of the surface terminating groups.

DOI: 10.1103/PhysRevB.82.195401 PACS number(s): 81.07.Bc, 78.67.Bf, 78.55.Ap, 61.72.Hh

I. INTRODUCTION

Silicon nanocrystals (NCs) are widely discussed as abundant and nontoxic absorber material in third generation photovoltaics,[1] silicon-based optoelectronic devices such as lasers[2] or light-emitting diodes[3] and nonvolatile memories.[4] Since the properties of nanostructures are much more influenced by their interfaces than bulk materials, the understanding of the interface and potential differences originating from different manufacturing parameters is crucial. The predominantly used matrix material for NCs is SiO_2 due to its high band gap and the well understood properties of the bulk Si/SiO_2 interface. One of the main process steps of most silicon nanocrystal manufacturing techniques is the high-temperature annealing to form Si clusters and to induce their crystallization. As one is dealing in essence with a Si/SiO_2 system, high vacuum is not an option for the annealing ambient because of the long known structural degradation driven by $SiO_{(g)}$ release at the Si/SiO_2 interface if carried out in an ambient of insufficient oxygen content (O_2 partial pressure, p_{O_2}, below the critical value).[5] The escaping SiO effectively leads to drastic degradation of the interface and a loss of Si. So, ideally, annealing should be carried out under sufficient p_{O_2} to block this reaction and insufficient p_{O_2} to avoid significant NC oxidation. The favored choice is N_2 or Ar, which in terms of NC properties was shown to make a difference.[6] The higher energetic photoluminescence (PL) observed for N_2 compared to Ar-annealed NC samples was previously attributed to the ability of nitrogen to suppress the diffusion of silicon atoms that form the Si clusters during annealing[7] or silicon consuming nitridation at the NC interface.[6] Very recently, we suggested an alternative explanation since it was observed that small NCs show a stronger N-blueshift than larger NCs.[8] This explanation is based on the influence of the incorporated nitrogen on the electronic structure of NC, which was modeled for various matrices by means of density-functional theory calculations.[9] The polarity of the surrounding matrix material is shown to dominate the NCs electronic structure if its size is <37 Å. For larger NCs mainly quantum confinement defines the highest occupied molecular orbital-lowest unoccupied molecular orbital (HOMO-LUMO) gap. Significantly higher PL emission energies were also reported for NCs in a Si_3N_4 compared to SiO_2 matrix.[10,11] Taking this into account, the blueshift from interfacial nitrogen should be more pronounced for small NCs (~2 nm) and less for larger ones (~5 nm).

Nitrogen is known to be not inert toward the Si/SiO_2 interface at high temperatures[12] whereas it cannot transform an oxide into a nitride. Therefore, the position of nitrogen incorporation was assumed to be the NC/SiO_2 interface.[6] By

means of time-of-flight secondary ion mass spectrometry (ToF-SIMS) measurements on thin ion-implanted SiNC layers annealed in N_2 a correlation of the N-related signal to the NC layer was reported.[13] However, resonant nuclear reaction analysis (RNRA) measurements using the $^{14}N(\alpha,\gamma)^{18}F$ nuclear reaction revealed a small quantity of N not only for N_2 annealed samples but also for samples annealed in Ar, which was attributed to coimplantation of N during the Si^+ implantation.[14] In this work the peak N concentration for N_2 annealed samples was reported to be about 0.7 at. % (average areal concentration 1×10^{16} N/cm^2). An intentional second N_2^+ implantation step (3 and 6×10^{16} N/cm^2) resulted in much less PL performance which suggests that a certain small amount of N incorporation improves the NC/SiO_2 interface quality[15] whereas an increased amount of N suppresses the NC growth and deteriorates the interface.[14] The improvement of the NC interface quality by N_2 versus Ar annealing was also quantified by electron-spin-resonance (ESR) measurements to about 50% less $P_{b(0)}$ and P_{b1} interface defects.[8] Further support for the idea of N incorporation at the NC interface comes from the fact that there is a one to two monolayers thick silicon suboxide transition shell at the NC/SiO_2 interface as has been demonstrated recently.[16] This nonstoichiometric oxide shell is presumably the only place of the sample system where N atoms can bond. In accordance to these results, N could act to passivate dangling Si-O bonds and might also lower interfacial strain.[17] However, in the formerly reported work the samples were manufactured by ion implantation and exhibit NCs distributed over the thin film according to the Si implantation profile and without precise control of size or position. Accordingly, analyzing the impact of the N on PL and interface defects as a function of the NC size and density was not possible. In this work, we will analyze the influence of interfacial N on NCs having a unique size control due fabrication by the SiO/SiO_2 superlattice approach.[18]

II. EXPERIMENTAL DETAILS

Two sample sets (P and E) were prepared in order to investigate the influence of N_2 annealing in comparison to Ar annealing. For sample set P six piranha cleaned (H_2SO_4 and H_2O_2, 70 °C, 10 min) *n*-type (100)-Si wafers were coated with superlattices consisting of 30 SiO_x/SiO_2 bilayer stacks in a thermal evaporator.[18] Deposition of SiO_x and SiO_2 was achieved by evaporation of SiO powder under high vacuum (1×10^{-6} mbar) or an O_2 pressure of 8×10^{-4} mbar, respectively. The respective stoichiometries are $x=1.2$ for SiO_x and $x=2.0$ for SiO_2. For all samples the SiO_2 layer thickness was 4 nm and each wafer was finally capped with 10 nm SiO_2. The SiO_x layer thickness in the bilayer stacks was varied from 1.5 to 6 nm and this value determines the sample name (e.g., the sample with 4 nm SiO_x thickness is labeled P4, etc.). Table I gives an overview of the structure of all samples used in this study. It should be noted that because of the good layer homogeneity pieces cut out of the wafer do not have significant thickness variations in the superlattice stack, hence they are comparable to each other. Due to the limited sample space in the ESR measurement cell (cavity) a second sample set (labeled E) was prepared on an only 75-μm-thick *p*-type Si wafer to increase the sample to substrate ratio and hence ESR signal sensitivity. This sample set consists of 45 SiO_x/SiO_2 bilayer stacks on each side of the double side polished wafer with 3/4 nm layer thickness, respectively. Pieces of each wafer were annealed at 1100 °C either in Ar or N_2 for 1 h in a quartz tube furnace equipped with a turbomolecular pump and electronically controlled pressure regulation. To account for the sensitivity of NCs to trace amounts of oxygen in the annealing atmosphere the furnace tube was evacuated to 1×10^{-6} mbar prior to establishing a N_2 or Ar gas flow of 50 SCCM at a constant pressure of 1050 mbar. Furthermore, the annealing system was checked for a negligible leak rate ($\sim10^{-5}$ mbar l/s^{-1}) and the employed gases (99.9999%) were additionally point-of-use purified to decrease impurities (i.e., O_2, H_2, and H_2O) to the ppb level. Thereby, an annealing ambient with a p_{O_2} is achieved that allows for the prevention of both significant NC oxidation and SiO_2 degradation. One half of each annealed sample was subsequently postannealed in pure H_2 ambient at 450 °C for 1 h to achieve NC/SiO_2 interface defect passivation. The suffix of the sample number specifies the annealing and postannealing treatment, e.g., P4-Ar (Ar annealing), E-N_2H_2 (N_2 annealing and subsequent H_2 treatment), etc.

TABLE I. Overview of the SiNC superstructures prepared for this work. Sample set E was especially dedicated to ESR measurements with one 45-bilayer stack evaporated on each side of the wafer.

Sample	P1.5	P2	P3	P4	P5	P6	E
Bilayer pairs	30	30	30	30	30	30	2×45
SiO_x thickness (nm)	1.5	2	3	4	5	6	3

Photoluminescence was measured on all samples with a LN_2-cooled charge coupled device camera attached to a single grating monochromator and a HeCd laser (3.8 eV line) as excitation source. All spectra were corrected for the spectral response of the setup. Time-resolved PL was measured at room temperature with the same monochromator and a photomultiplier tube (Hamamatsu R5108) under excitation of a pulsed nitrogen laser (337 nm). The luminescence decay was measured at the peak wavelength of each sample with a resolution of 0.5 μs. Bright-field transmission electron microscopy (TEM) cross-section micrographs were obtained with a CM20-T operated at 200 kV. High angle annular dark-field imaging (HAADF) in scanning TEM mode was done with a FEI TITAN 80-300 equipped with an electron energy-loss spectroscopy (EELS) detector. A JEM-4010 (400 kV) was used for high-resolution TEM (HRTEM). Elastic recoil detection analysis (ERDA) was carried out using 35 MeV $^{35}Cl^{7+}$ projectiles from a 5 MV tandem accelerator. The scattering angle was 31°, the angle between beam and sample normal 75°. Recoiled target ions were detected by a Bragg-ionization chamber. The hydrogen ions were detected separately under 38° by a surface barrier detector with an 18 μm Al-foil entrance window. WINDF was used to simulate the measurements.[19] Stoichiometries of the SiO_x thin films were

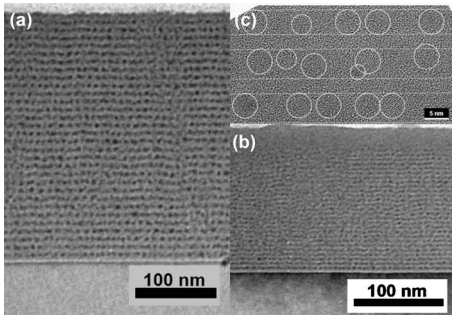

FIG. 1. Cross-sectional bright-field TEM images of samples (a) P6-Ar and (b) P3-N_2 as well as an HRTEM image of sample (c) P6-N_2. The horizontal lines are a guide to the eyes to indicate the SiNC/SiO_2 layer structure. Circles indicate Si nanocrystals that are represented by the (111)-lattice fringes.

determined by Rutherford backscattering (RBS) with 2 MeV He^+ projectiles under a detection angle of 170°. The measurements were modeled by Rutherford backscattering spectrometry analysis package (RUMP). A ToF-SIMS (ION-TOF GmbH) was used to investigate the elemental composition of the nanocrystal superlattice structure. The depth profile measurements were performed using a Cs^+ ion sputter source operated at 1 keV and 75 nA. The analysis was carried out under negative polarity using a pulsed Ga^+ ion beam at 15 keV and 1 pA. An electron flood gun was used to compensate for sample charging. However, close to the superlattice/wafer interface this charge compensation was not fully sufficient explaining the slight distortion of the signals. Sample E was cut into ESR-compatible slices (2×9 mm^2) of which cutting damage and backside oxide were removed by wet chemical etch (CP4) prior to ESR probing. A typical ESR sample stack was comprised of ~20 slices of double-side-coated substrate, summing up to a total sample area of ~7.2 cm^2. Conventional cw ESR investigations were carried out at 4.2 K using a K-band (~20.6 GHz) spectrometer driven in the adiabatic mode.[20] The applied microwave power (P_μ) and amplitude of the sinusoidal modulation (~100 kHz) of the static magnetic field (**B**) were cautiously reduced to avoid signal distortion. A comounted calibrated Si:P marker sample [$g(4.2\ \mathrm{K})=1.99869$] was used for g value and defect density determination. The attained absolute and relative accuracies on the latter were estimated to be ~20% and ~10%, respectively.

III. RESULTS AND DISCUSSION

A. Presence of N at the NC/SiO_2 interface

Figure 1 shows two representative cross-section bright-field TEM images of samples (a) P6-Ar and (b) P3-N_2 that demonstrate the expected superlattice structure. Irrespective of the annealing ambient the samples with small NCs (P1.5–P3) contain 28–29 NC layers whereas the larger NC samples (P4–P6) show the full amount of 30 layers. Sometimes, there is a reduced contrast of the topmost NC layer which makes it difficult to count the correct number of layers. This is most likely attributed to a full or partial oxidation of the topmost NC layer despite the high purity of the annealing system. Since the small NCs comprise of only a few hundred Si atoms they are more susceptible to elimination by oxidation than the larger NCs comprised of several thousand Si atoms. As a second observation from the analysis of the TEM images, the measured sample thickness is in average $(89\pm 4)\%$ of the intended thickness preset by the quartz crystal microbalance in the evaporator. We attribute this to a compaction of the reactively evaporated and therefore not completely dense SiO_x ($1.2\leq x\leq 2$) material, which also leads to a ~10 times higher etch rate in buffered HF for as-prepared compared to annealed SiO_2 layers as measured by ellipsometry.

Samples P2, P4, and P6 were furthermore studied by HRTEM in order to determine the average NC size (see Table II). Figure 1(c) depicts an HRTEM image of P6-N_2. The superlattice structure is clearly visible. Please note, the NCs are randomly oriented in the layer, so only those having (111) orientation respective to the electron beam can be imaged. Because of the finite thickness of the TEM specimen these images are not representative to determine the NC spacing: two NCs could appear to be in contact with each other in the projection although they separated in the z dimension. In addition, the TEM specimen preparation (particularly the final ion milling) can result in an amorphization or cutting of NCs which explains that some NCs appear much smaller than the average. No size difference could be observed for Ar and N_2 annealed samples, though, due to the rather large NC size uncertainties from TEM analysis and the expected small size differences, this does not unequivocally rule out the assumption of growth suppression for N_2 annealing.

Representative for all samples P4-N_2 was investigated by HAADF (also referred to as Z-contrast imaging) and EELS. Figure 2 shows a HAADF image where due to the ~Z^2 proportionality of the intensity, light gray colors account for Si-rich areas, i.e., NCs of about 3.5–4 nm in diameter and ~3.5–4 nm apart. EELS line scans reveal the Si L_{23} edge to obtain the fine structure of SiO_2 as well as a Si-enriched layer around the Si cores, which is regarded to be the suboxide transition shell investigated before.[16] No nitrogen could be traced by EELS indicating a concentration below the detection limit.

The PL spectra of samples P1.5 and P6 (Ar and N_2 annealed) are exemplary shown in Fig. 3. As reported before the blueshift caused by N_2 compared to the Ar annealing is pronounced for small NCs (here ~2 nm) and insignificant for large NC samples (here ~6 nm).[8] The analysis of all PL spectra (Fig. 4) reveals a similar behavior: N_2 annealed samples are always stronger in terms of PL peak intensity and depending on the NC size more or less blueshifted compared to the samples annealed in Ar. In Fig. 4(c) the peak energy difference between N_2 and Ar annealing is presented. Although the data points are somewhat scattered the trend of higher N-blueshift for smaller NCs is obvious and highlighted by the linear fit. The full width at half maximum (FWHM) values are about 140 nm for the samples P1.5 and P2 and slightly larger for P5 and P6 (155–160 nm). These intense and virtually symmetric PL curves with peaks from

TABLE II. Elemental composition derived from ERDA measurements of samples P2, P4, and P6. The geometrical quantities arise from the model depicted in Fig. 9. Numbers in parentheses refer to formulas used in the text.

Sample	P2-N_2	P4-N_2	P6-N_2
Total sample atoms: N_t (cm^{-2})	$(9.56 \pm 0.1) \times 10^{17}$	$(1.12 \pm 0.01) \times 10^{18}$	$(1.67 \pm 0.02) \times 10^{18}$
Si content: N_{Si} (at. %)	35.9 ± 1	37.4 ± 1	41.6 ± 1
O content: N_O (at. %)	62.5 ± 1	61.0 ± 1	56.9 ± 1
N content: N_N (at. %)	0.99 ± 0.1	1.43 ± 0.1	1.16 ± 0.1
Contribution of suboxide transition shell: y (at. %), Eq. (7)	1.3 ± 0.2	1.9 ± 0.2	3.6 ± 0.2
Excess Si: $N_{ex\text{-}Si\%}$ (at. %)	4.0 ± 0.3	6.0 ± 0.3	11.4 ± 0.6
Excess Si: $N_{ex\text{-}Si}$ (cm^{-2}), Eq. (3)	$(3.8 \pm 0.3) \times 10^{16}$	$(6.7 \pm 0.3) \times 10^{16}$	$(1.9 \pm 0.1) \times 10^{17}$
NC diameter: d_{NC} (nm)	2.0 ± 0.25	3.5 ± 0.25	5.25 ± 0.25
NC volume: V_{NC} (nm^3), Eq. (4)	4.2 ± 1.6	22.4 ± 4.8	75.8 ± 10.8
Si atoms per NC: $Si_{at/NC}$	209 ± 79	1122 ± 241	3788 ± 542
Areal NC density: N_{ad} (cm^{-2}), Eq. (5)	$(6.3 \pm 3) \times 10^{12}$	$(2.1 \pm 0.6) \times 10^{12}$	$(1.7 \pm 0.4) \times 10^{12}$
NC spacing: d_{SiO_2} (nm), Eq. (6)	1.9 ± 0.7	3.2 ± 0.5	2.0 ± 0.3
NC surface area: A_{NC} (nm^2)	12.6 ± 3.2	38.5 ± 5.5	86.6 ± 8.2
Total inner NC interface area per square centimeter sample: $A_{total}(cm^2)$, Eq. (8)	23.0 ± 17.1	23.4 ± 10.4	42.7 ± 14.8
N per NC interface (cm^{-2})	$(3.9 \pm 3.3) \times 10^{14}$	$(6.6 \pm 3.4) \times 10^{14}$	$(4.4 \pm 1.9) \times 10^{14}$

1.3 to 1.6 eV indicate the good NC size control obtained by the superlattice approach[21] but also demonstrate the limitations of size control for the smallest NCs. From Fig. 4(a) it is obvious that the initial SiO_x layer thicknesses of 1.5 and 2 nm result in similar PL emission energies, however, the PL intensity for P1.5 is lower [Fig. 4(b)]. This can be explained by the critical nucleation radius for Si nanocrystals in SiO_2 (approximately 1.6 nm); smaller Si clusters do not crystallize whatever the annealing temperature.[22] An initial SiO_x layer thickness of less than this minimum NC size results in the same lowest-limit NC diameters but due to the reduced amount of excess Si also in a smaller NC areal density and hence the sample exhibits reduced PL intensity at the same peak position. The distribution of the PL intensity values is according to our experience. The middle-size NCs (3–4 nm) show the most intense peaks while both the smallest and largest NCs have about half of this intensity [Fig. 4(b)]. Generally, this behavior can be attributed to a trade off between the absorption cross section and the areal NC density per superlattice layer. The larger NCs have a larger cross section but their over all PL intensity diminishes due to the smaller amount of NCs per unit area. For the smallest NCs the areal density is high but the excitation cross section is small. In addition, the efficiency of the radiative decay has to be considered which depends on the NC size. All these factors seem to compensate each other in a way that the middle-sized NCs always emit the highest PL intensities. It is worth noting that the excitation power of the unfocused laser spot used here was ~0.1 mW (~2 mW cm^{-2}) to rule out any PL satura-

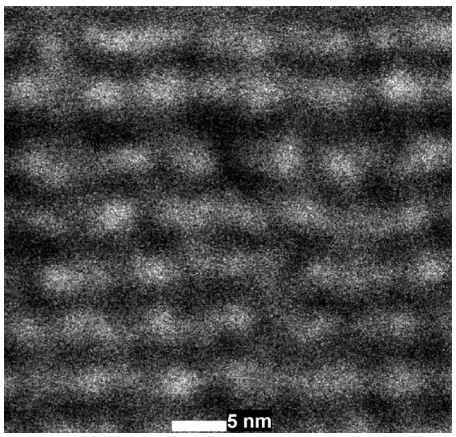

FIG. 2. HAADF image of sample P4-N_2 obtained in scanning TEM mode. The NCs appear to be of spherical shape with diameters of ~3.5 nm and likewise spacing.

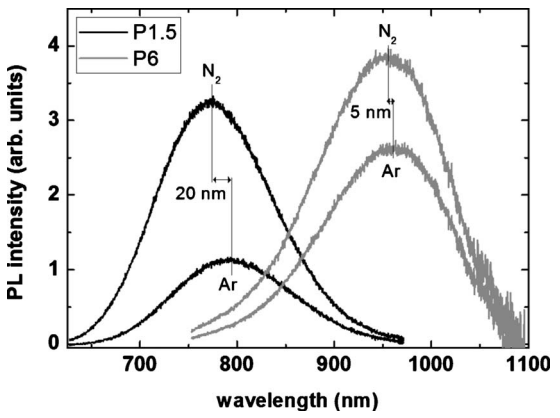

FIG. 3. PL spectra of samples with smallest (P1.5) and largest NCs (P6) with respect to the sample set used here. The blueshift from N_2 vs Ar annealing is clearly visible only for small NCs.

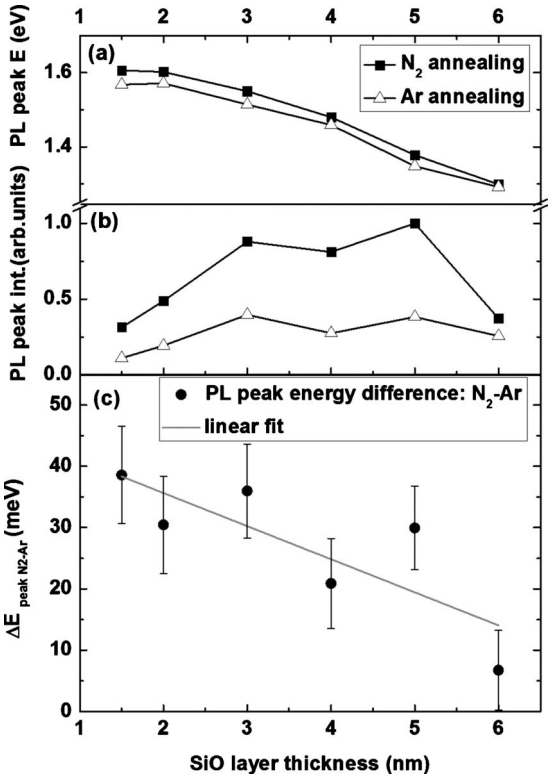

FIG. 4. Analysis of the PL peaks of sample set P. (a) The peak-positions shift continuously with the initial SiO layer thickness from 1.3 to 1.6 eV. (b) Generally, N_2 annealing yields higher PL intensities than Ar. (c) The peak energy difference of N_2-Ar annealing (N-blueshift) shows a decreasing trend with NC size.

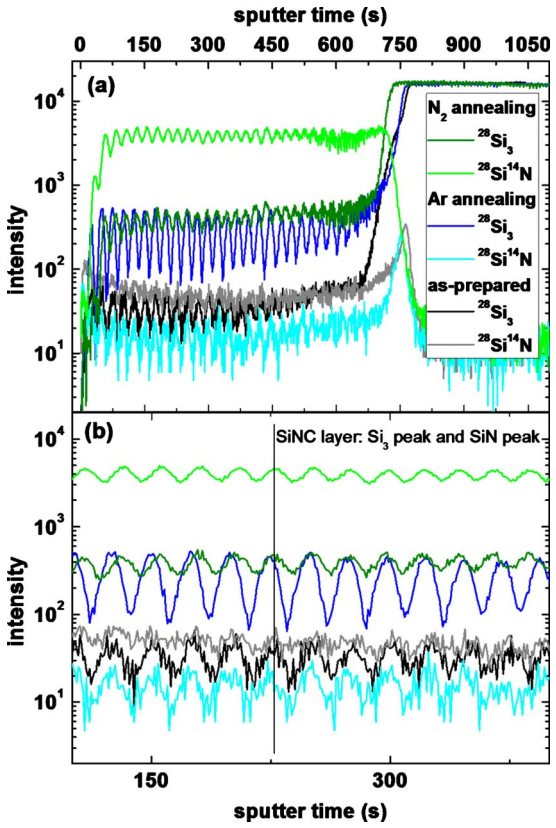

FIG. 5. (Color online) ToF-SIMS depth profiles of selected ions ($^{28}Si_3^-$, $^{28}Si^{14}N^-$) of sample P5 (as-prepared, N_2 and Ar annealed). (a) The $^{28}Si_3^-$ oscillations clearly indicate the NC layers. (b) A significant $^{28}Si^{14}N^-$ signal is only present for the N_2 annealed sample (light green) and its oscillations are in phase with the $^{28}Si_3^-$ signal oscillations (dark green), verifying the accumulation of N in the NC layers.

tion effects due to Auger processes.[23,24] Furthermore, it should be mentioned that the assignment made above does not account for the contribution of nonradiative defects to I_{PL}. A study on the dependence of defect types and density on the NC size is in progress.

ToF-SIMS depth profiles of selected ions ($^{28}Si_3^-$ and $^{28}Si^{14}N^-$) measured on sample P5 in its three different states (as-prepared, N_2, and Ar annealed) are presented in Fig. 5. All signals are normalized to the $^{28}Si_3^-$ signal in the Si substrate. Besides the signals shown and some other Si-O-N compounds no other impurity masses were detected. After some surface-related signal distortions, Fig. 5(a) shows ~30 oscillations of the $^{28}Si_3^-$ signal, which are clearly related to the Si nanocrystal layers where silicon atoms bound to more than one silicon atom (Si_n, $n \geq 2$) are present, i.e., in contrast to the SiO_2 layers. It should be noted that the oscillation distortions close to the substrate interface are related to insufficient charge compensation despite the use of the electron flood gun. Hence these distortions do not reveal this region as being a distorted superlattice structure in accordance with TEM observations. The extremely weak $^{28}Si_3^-$ and $^{28}Si^{14}N^-$ signals in the as-prepared sample (black and gray curves) demonstrates both the absence of Si clusters in the not-annealed SiO_x layers as well as the absence of nitrogen. Nevertheless, some shallow oscillations of the $^{28}Si_3^-$ intensity (black) between the Si-rich SiO_x and the SiO_2 layers can be seen. After annealing the $^{28}Si_3^-$ signal intensity (blue and dark green) increases by one order of magnitude which corresponds to the formation of nanocrystalline Si phases. In addition, a very strong $^{28}Si^{14}N^-$ signal (light green) occurs for the sample annealed in N_2 but not for Ar (cyan curve). The magnified profile detail in Fig. 5(b) shows clearly that the peaks of $^{28}Si^-$ and $^{28}Si^{14}N^-$ are in phase, i.e., the nitrogen is incorporated significantly only in the NC layers. This incorporated nitrogen may be the reason for the half as high peak to valley ratio of the $^{28}Si^-$ intensity of the N_2-annealed sample (dark green) compared to the Ar-annealed sample (blue).

In order to investigate the properties of the NC/SiO_2 interface in detail sample E was specially prepared to maximize the NC volume in the ESR cavity. The two common $P_{b(0)}$ and P_{b1} interface defects and the SiO_2-related EX center occur in all four states of sample E, i.e., E-N_2, E-Ar, E-N_2H_2, and E-ArH_2. Details on the structure and relevance of these three prominent defects have been published elsewhere.[8,25–28] From previous measurements it has also been established that samples not subjected to (post)annealing in H_2 do not contain any unintended hydrogen as was investigated by defect activation studies by means of vacuum ultraviolet irradiation.[28,29] Figure 6 shows the observed defect densities in the respective states of sample E. The inset of Fig. 6 shows the measured PL spectra with the attendant

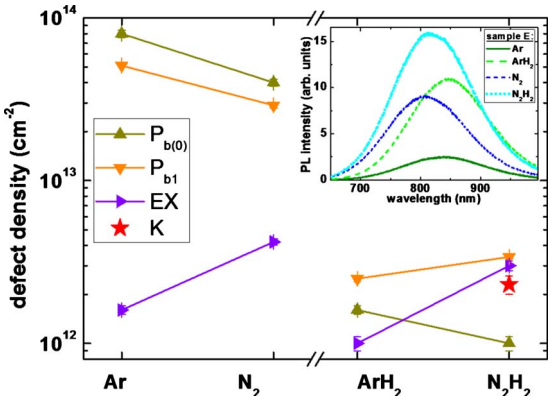

FIG. 6. (Color online) Paramagnetic defect densities derived from ESR measurements on sample E. The amount of NC/SiO_2 interface defects (i.e., P_{b0} and P_{b1}) is reduced for N_2 annealing and almost complete passivation is observed after H_2 treatment. The most important feature is the detection of the K^0 center (modeled as $^{\bullet}Si \equiv N_3$) for sample E-N_2H_2 which reveals the presence of N at the NC interface. In the case of sample E-N_2, the signal could not be resolved due to the overlap of intense signals of the other copresent defects. The inset shows the PL spectra for all four states of sample E for reference.

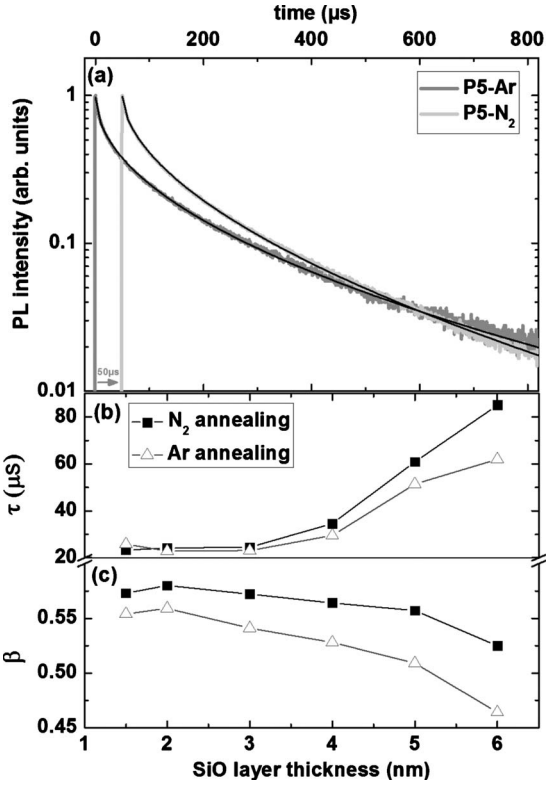

FIG. 7. (a) PL decay of samples P5-Ar and P5-N_2, the black lines are the stretched exponential fits. For the sake of clarity the curve of P5-N_2 (light gray) was shifted 50 μs to the left. The results of all stretched exponential fits of sample set P are given below: (b) luminescence lifetime τ and (c) dispersion factor β.

N-related blueshift and change in the intensity as described above for sample set P. As has been reported before N_2 annealing is beneficial since about half the amount of P_b-type defects are measured compared to Ar annealing.[8] However, the EX density is higher after N_2 annealing, which is not supposed to heavily influence the NC properties due to the SiO_2 related nature of this defect. After H_2 passivation the defect densities are in average ~50 times reduced for $P_{b(0)}$ and ~15 times for P_{b1} whereas the EX density reduction is only ~33%. The most important result from our ESR measurement is the detection of the K^0 center in sample E-N_2H_2. This paramagnetic defect is modeled as an unpaired electron on a Si atom bonded to three N atoms ($^{\bullet}Si \equiv N_3$) with $g_c = 2.003 \pm 0.0003$.[30,31] Since the other defect signals are relatively intense the K^0 center could not be resolved for the not H_2-passivated sample E-N_2 but the absence of this signal for sample E-ArH_2 verifies its identification. The K^0 center density was determined to be $(2.3 \pm 0.3) \times 10^{12}$ cm^{-2}. Since the PL peak position and therefore the NC size of sample E is close to that of sample P4 we can estimate that there are $\sim 2 \times 10^{12}$ NCs cm^{-2} per layer (see Sec. III B and Table II). With 45 NC layers on each side of the sample there are in total $\sim 1.8 \times 10^{14}$ NCs cm^{-2}, i.e., about one K^0 center per ~80 NCs (after H_2 passivation annealing). The presence of the K^0 center unequivocally demonstrates the incorporation of N atoms right at the NC/SiO_2 interface for N_2-annealed samples.

B. Absence of growth suppression by N_2 annealing

The exciton confinement energy has a nonlinear dependence on the quantum dot size.[32] Therefore, it is evident that a constant relative NC size offset by N_2 annealing (according to Refs. 6 and 14) results in a pronounced effect on the band gap for small NCs, which could also account for the size-dependent N-blueshift shown in Fig. 4(c). Time-resolved PL has been performed at the peak wavelength of each sample to check for differences in the decay time (τ) of N_2 and Ar-annealed samples (Fig. 7). As shown exemplary for samples P5 in Fig. 7(a) the experimental data were fitted by a stretched exponential function

$$I(t) = I_0 \exp[-(t/\tau)^{\beta}]. \quad (1)$$

Since the required phonon contribution to the luminescence decay of an exciton is decreased for decreasing NC size the time constant τ is generally decreasing as well.[21] This behavior is consistent with the τ data in Fig. 7(b). However, the assumption of smaller NCs in case of N_2 annealing (due to growth suppression) and thereby shorter PL lifetime is not evident. In contrast, the decay time τ is even longer for large NCs (P4–P6) while for small NC samples (P1.5–P3) equal time constants were measured. The similar lifetimes for the small NCs despite a pronounced N-blueshift in PL indicate identical size. The drastic difference in lifetime of 10–20 μs for the large NCs (revealing a very weak-annealing ambient dependence in terms of N-blueshift) is supposed to have its origin in the nonradiative defects. Since Ar compared to N_2 annealing results in approximately twice the amount of NC/SiO_2 interface defects[8] the luminescence lifetime should be shorter.[33] It is also established that large NCs are more prone to have nonradiative defects that quench their PL.[34]

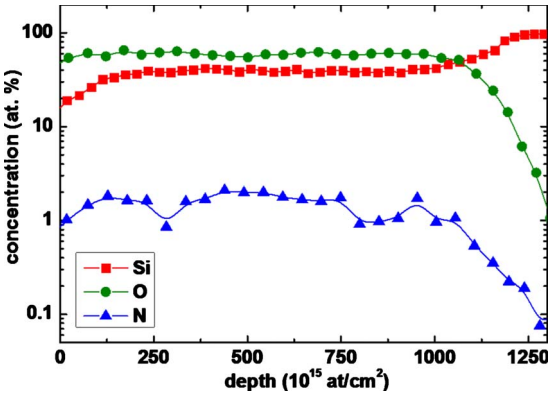

FIG. 8. (Color online) ERDA depth profile of sample P4-N_2. The average N concentration was determined to ~1.4 at. % and the Si/O ratio to 37.4/61.0 at. %.

Therefore, the redshift observed after full inactivation of interface defects (by H_2 treatment) is pronounced for large NCs. Assuming a sample system comprised of an ensemble of slightly different NC diameters, excitons tend to migrate to the larger NCs where they experience a higher probability for a nonradiative decay. Given the fact that N_2 annealing reduces defects the lifetime increase is pronounced for samples with large NCs (here P4–P6). However, this argumentation could also implicate that the observed small N-blueshift is a result of compensation by the accompanied redshift due to defect passivation by N_2 annealing. All in all, the bare examination of lifetimes cannot solve the question about the role of N_2 annealing.

The dispersion factor β derived from Eq. (1) is plotted in Fig. 7(c). With increasing NC size β decreases while the difference in the dispersion factors between the two annealing atmospheres slowly increases. Among the various interpretations of the dispersion factor (Ref. 35 and references therein) we will attribute it to exciton migration between a disordered system of interconnected nanocrystals.[36] It was shown for H_2 annealing that β increases with proceeding defect passivation.[33] Again the offset between the dispersion factors of the two annealing ambients can be interpreted as an effect of the improved interface quality by N_2 annealing. The reduced defect density results in increased exciton migration between radiative NCs. In contrast, exciton migration between NCs with a higher density of nonradiative defects (here Ar-annealed samples) increases the probability of luminescence quenching, i.e., these migrated excitons do not contribute to the PL signal. Alternatively, the higher β may be attributed to the interfacial N that could act as a barrier improvement against exciton migration compared to a N-free interface. The overall trend to lower β values for increasing NC size is attributed to increasing exciton migration between NCs of different lifetimes, i.e., of slightly broader size distribution, as represented by the slightly broader FWHMs for samples with larger NCs (see Sec. III A).

For quantification of the amount of nitrogen as well as the elemental composition, samples P2, P4, and P6 were investigated by ERDA. Figure 8 shows the depth profile of sample P4-N_2. In Table II the results for all three N_2-annealed samples are summarized. P4-Ar and P4-N_2H_2 were also measured, where, reassuringly, in the Ar-annealed sample the virtual absence of N was demonstrated: (0.09 ± 0.1) at. %, consistent with the ToF-SIMS data (Fig. 5). In contrast, for the other samples the N content is clearly identified in the range of $(1-1.4 \pm 0.1)$ at. %. However, the amount of H was in all samples indistinguishably, determined to an average of (0.14 ± 0.1) at. %. So besides H from, e.g., of surface contaminations (hydrocarbons) the additional H in the H_2 post-annealed sample (P4-N_2H_2) seems to be below the detection limit of ERDA.

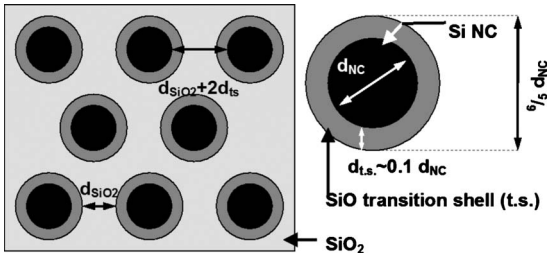

FIG. 9. Schematic of the NC/transition shell model developed to analyze the ERDA data given in Table II.

By means of a geometrical model the areal density of NCs and the amount of interfacial N at the NC surface can be estimated (Table II). The average NC diameters d_{NC} are derived from HRTEM analysis (Sec. III A). Instead of simply calculating the excess Si atoms for a complete decomposition into Si and SiO_2 the substoichiometric transition shell surrounding the NC has also to be taken into account. Therefore, the NC will be treated as a Si sphere with a suboxide transition shell of an average stoichiometry $SiO_{x=1}$ with a thickness of 10% of its diameter (according to Ref. 16) surrounded by a SiO_2 matrix in a regular array for each of the layers in the superlattice. A schematic of this model as well as the symbols used is shown in Fig. 9. The resulting volume of the transition shell is

$$V_{ts} = 1/6\pi[(6/5d_{NC})^3 - d_{NC}^3] = 91/125 \times V_{NC}. \quad (2)$$

The variable y is introduced as the amount of Si and O in the transition shell volume. It is subtracted equally from N_{Si} and N_O resulting in

$$N_{ex\text{-}Si} = N_{ex\text{-}Si\%} \times N_t = N_{Si} - 1/2(N_O + y). \quad (3)$$

The NC volume is calculated by

$$V_{NC} = 1/6\pi d_{NC}^3 \quad (4)$$

and the lattice spacing of 0.543 nm for the bulk Si fcc diamond crystal structure allows for 50 Si atoms nm^{-3}. Under the assumption of in average (29 ± 0.5) NC layers (Sec. III A and Fig. 1) the areal NC density per layer can be calculated by

$$N_{ad} = N_{ex\text{-}Si}/(29 \times Si_{at/NC}). \quad (5)$$

Thereby, the average spacing of the NCs can be approximated. The assembly of the two-dimensional array of spherical NCs is assumed to be hexagonal, resulting in a packing density of $\pi/(2 \times \sqrt{3}) = 90.7\%$. We will define the distance

between the NC including their transition shell as d_{SiO2}, which can be calculated by

$$d_{SiO_2} = 3^{-1/4} \times \sqrt{(2/N_{ad})} - 6/5 d_{NC}. \quad (6)$$

Please note that to find distance between two NC cores the transition shell thickness has to be added: $d_{SiO_2}+2d_{ts}$. The total volume of the transition shell V_{ts} can be estimated to $(2y \times N_t)/23$, when the atomic density of SiO is $\sim 2.3 \times 10^{22}$ cm^{-3}=23 nm^{-3} (value taken from SiO_2). Using this result for V_{ts} and inserting it together with Eq. (4) into Eq. (2), the contribution of the suboxide transition shell to the excess Si content can be calculated

$$y = 230/843 N_{Si} - 115/843 N_O. \quad (7)$$

The total NC/SiO_2 interface area per square centimeter sample material can be estimated to

$$A_{total} = \pi d_{NC}^2 \times 29 N_{ad}. \quad (8)$$

Finally, the measured amount of N can be treated as being distributed over the whole inner interface area: $(N_N \times N_t)/(A_{total}+1\ \text{cm}^2)$, where the addition of 1 cm^2 accounts for the planar interface to the Si substrate, which is also supposed to incorporate N.[17] The results are shown in Table II and under the assumptions mentioned above it turns out that in average 5×10^{14} N atoms cm^{-2} NC surface occur which corresponds to ~75% of a Si monolayer. This value ($\sim 5 \times 10^{14}$ N atoms/cm^2) has been reported before to be apparently the optimum value for bulk planar Si/SiO_xN_y interfaces.[37] Hence, with the data presented here we can again draw a direct comparison between the properties of the NC/SiO_2 interface and the bulk-Si/thermal SiO_2 interface, as has also been done before in terms of paramagnetic interface defect densities.[29] It should be noted that the uncertainties ascribed to d_{NC} cause mathematically rather high and partially unrealistic uncertainties for all derived quantities due to square and cubic dependencies. An additional point that should be mentioned concerns the actual shape of NCs, which was recently shown on samples without size control to be not necessarily always spherical but could also involve complex morphologies.[38]

The discovery of N incorporation in the order of magnitude of only one monolayer contradicts the assumption of a Si consuming nitridation of the NCs resulting in reduced size and blueshifted PL (Ref. 6). Furthermore, the idea of reduced NC size due to diffusion suppression by the presence of nitrogen[7,14] does not account for the diffusion mechanism and its dynamics. The main mechanism of SiO phase separation has been recently identified as the emission of oxygen and its outdiffusion into the SiO_2 resulting in the formation of Si precipitates.[39] Moreover, it has been shown that this process takes place at time scales of seconds for temperatures of 1000 °C (Ref. 39 and references therein). That means the phase separation and Si clustering is already accomplished when the main annealing temperature of typically 1100 °C is reached (assuming conventional furnaces with ramp rates in the range of 10 °C/min), i.e., the temperature and time needed to enable nitrogen to diffuse into the NC layers and to effect NC growth suppression is just not provided.

These arguments support the explanation that the interfacial nitrogen from N_2 annealing influences the electronic structure of the NC and its HOMO-LUMO gap. Since the polarity of the Si-N bond is smaller than that of the Si-O bond the band-gap energy increases.[9] The NC with interfacial N experiences a surrounding matrix partially comprised of nitride bonds and therefore decreased polarity. Merely NCs < 37 Å have an electronic structure which is controlled significantly by its surface terminating groups[9] therefore the N-blueshift in PL is pronounced only for samples with small NCs.

IV. CONCLUSIONS

In summary, the presence of N at the NC/SiO_2 interface has been demonstrated by the observation of the K^0 center ($^{\bullet}Si \equiv N_3$) by ESR. This provides evidence that N is incorporated at the interface between the NC and its suboxide transition shell. By means of a sample set of size-controlled Si nanocrystals (1.3–1.6 eV PL peak emission energy) a clear trend of N-related PL blueshift with decreasing NC size was evidenced. Time-resolved PL measurements show different characteristics of τ and β for N_2 and Ar annealing that might be related to the ability of N to partially passivate defects. However, similar PL lifetimes of the samples with small NCs indicate identical sizes despite pronounced N-blueshift. ERDA results are used to develop a geometrical model for the NCs that allows the approximation of the NC areal density and the total inner NC/SiO_2 interface area. In combination with the measured amount of N a coverage of $\sim 5 \times 10^{14}$ N/cm^2 interface could be estimated, which meets the supposed optimum amount of N for passivation at the bulk Si/SiO_2 interface. This result appears to disqualify the previously suggested explanation for the PL blueshift by N_2 annealing. The submonolayer of N cannot be interpreted as Si consuming nitridation of the NC. Si diffusion suppression by the presence of nitrogen was also discussed as origin of this N-blueshift. But this explanation does not consider the recently modeled Si clustering and its dynamics (emission and out diffusion of oxygen) which takes place much faster (time scale of seconds) and at lower temperatures than N diffusion. For these reasons, we attribute the N-blueshift to a reduction in the polarity of the surface terminating groups by the interfacial N and thereby an increased HOMO-LUMO gap.

ACKNOWLEDGMENT

This work was financially supported by the German Research Foundation (Grant No. ZA191/27-1).

[1] G. Conibeer, M. Green, R. Corkish, Y. Cho, E. C. Cho, C. W. Jiang, T. Fangsuwannarak, E. Pink, Y. Huang, T. Puzzer, T. Trupke, B. Richards, A. Shalav, and K. Lin, Thin Solid Films **511**, 654 (2006).
[2] L. Pavesi, L. Dal Negro, C. Mazzoleni, G. Franzò, and F. Priolo, Nature (London) **408**, 440 (2000).
[3] N. Lalic and J. Linnros, J. Lumin. **80**, 263 (1999); G. Franzò, A. Irrera, E. C. Moreira, M. Miritello, F. Iacona, D. Sanfilippo, G. Di Stefano, P. G. Fallica, and F. Priolo, Appl. Phys. A: Mater. Sci. Process. **74**, 1 (2002).
[4] S. Tiwari, F. Rana, H. Hanafi, A. Hartstein, E. F. Crabbé, and K. Chan, Appl. Phys. Lett. **68**, 1377 (1996).
[5] R. E. Walkup and S. I. Raider, Appl. Phys. Lett. **53**, 888 (1988); Y. Takakuwa, M. Nihei, and N. Miyamoto, Jpn. J. Appl. Phys., Part 2 **32**, L480 (1993).
[6] A. R. Wilkinson and R. G. Elliman, J. Appl. Phys. **96**, 4018 (2004).
[7] V. Mulloni, P. Bellutti, and L. Vanzetti, Surf. Sci. **585**, 137 (2005).
[8] D. Hiller, M. Jivanescu, A. Stesmans, and M. Zacharias, J. Appl. Phys. **107**, 084309 (2010).
[9] D. König, J. Rudd, M. A. Green, and G. Conibeer, Phys. Rev. B **78**, 035339 (2008).
[10] J. Barreto, M. Perálvarez, A. Morales, B. Garrido, J. Montserrat, and C. Domínguez, J. Mater. Res. **23**, 1513 (2008).
[11] M. S. Yang, K. S. Cho, J. H. Jhe, S. Y. Seo, and J. H. Shin, Appl. Phys. Lett. **85**, 3408 (2004).
[12] S. I. Raider, R. A. Gdula, and J. R. Petrak, Appl. Phys. Lett. **27**, 150 (1975).
[13] M. Perego, S. Ferrari, M. Fanciulli, G. B. Assayag, C. Bonafos, M. Carrada, and A. Claverie, J. Appl. Phys. **95**, 257 (2004).
[14] M. Bolduc, G. Genard, M. Yedji, D. Barbe, F. Martin, G. Terwagne, and G. G. Ross, J. Appl. Phys. **105**, 013108 (2009).
[15] P. Aubert, H. J. von Bardeleben, F. Delmotte, J. L. Cantin, and M. C. Hugon, Phys. Rev. B **59**, 10677 (1999).
[16] A. Zimina, S. Eisebitt, W. Eberhardt, J. Heitmann, and M. Zacharias, Appl. Phys. Lett. **88**, 163103 (2006).
[17] M. L. Green, T. Sorsch, L. C. Feldman, W. N. Lennard, E. P. Gusev, E. Garfunkel, H. C. Lu, and T. Gustafsson, Appl. Phys. Lett. **71**, 2978 (1997).
[18] M. Zacharias, J. Heitmann, R. Scholz, U. Kahler, M. Schmidt, and J. Bläsing, Appl. Phys. Lett. **80**, 661 (2002).
[19] N. P. Barradas, C. Jeynes, and R. P. Webb, Appl. Phys. Lett. **71**, 291 (1997).
[20] A. Stesmans, Phys. Rev. B **48**, 2418 (1993).
[21] J. Heitmann, F. Müller, L. X. Yi, M. Zacharias, D. Kovalev, and F. Eichhorn, Phys. Rev. B **69**, 195309 (2004).
[22] M. Zacharias and P. Streitenberger, Phys. Rev. B **62**, 8391 (2000).
[23] D. Kovalev, H. Heckler, G. Polisski, and F. Koch, Phys. Status Solidi B **215**, 871 (1999).
[24] D. Kovalev, J. Diener, H. Heckler, G. Polisski, N. Künzner, and F. Koch, Phys. Rev. B **61**, 4485 (2000).
[25] C. R. Helms and E. H. Pointdexter, Rep. Prog. Phys. **57**, 791 (1994).
[26] A. Stesmans and V. V. Afanas'ev, Phys. Rev. B **57**, 10030 (1998).
[27] A. Stesmans and F. Scheerlinck, Phys. Rev. B **50**, 5204 (1994).
[28] M. Jivanescu, A. Stesmans, and M. Zacharias, J. Appl. Phys. **104**, 103518 (2008).
[29] A. Stesmans, M. Jivanescu, S. Godefroo, and M. Zacharias, Appl. Phys. Lett. **93**, 023123 (2008).
[30] P. M. Lenahan and S. E. Curry, Appl. Phys. Lett. **56**, 157 (1990).
[31] W. L. Warren and P. M. Lenahan, Phys. Rev. B **42**, 1773 (1990).
[32] N. A. Hill and K. B. Whaley, Phys. Rev. Lett. **75**, 1130 (1995).
[33] A. R. Wilkinson and R. G. Elliman, Phys. Rev. B **68**, 155302 (2003).
[34] S. Cheylan and R. G. Elliman, Appl. Phys. Lett. **78**, 1225 (2001).
[35] J. Linnros, N. Lalic, A. Galeckas, and V. Grivickas, J. Appl. Phys. **86**, 6128 (1999).
[36] L. Pavesi, J. Appl. Phys. **80**, 216 (1996).
[37] E. P. Gusev, H. C. Lu, T. Gustafsson, E. Garfunkel, M. L. Green, and D. Brasen, J. Appl. Phys. **82**, 896 (1997).
[38] A. Yurtsever, M. Weyland, and D. A. Muller, Appl. Phys. Lett. **89**, 151920 (2006).
[39] A. Sarikov, V. Litovchenko, I. Lisovskyy, I. Maidanchuk, and S. Zlobin, Appl. Phys. Lett. **91**, 133109 (2007).